Lawrence Berkeley National Laboratory
Recent Work

Title
Understanding cation effects in electrochemical CO2 reduction

Permalink
https://escholarship.org/uc/item/1m78w0xw

Journal
Energy and Environmental Science, 12(10)

ISSN
1754-5692

Authors
Ringe, S
Clark, EL
Resasco, J
et al.

Publication Date
2019-10-01

DOI
10.1039/c9ee01341e

Peer reviewed

Understanding Cation Effects in Electrochemical CO$_2$ Reduction

Stefan Ringe[1,2,a,b], Ezra L. Clark[3,4,b], Joaquin Resasco[5], Amber Walton[3], Brian Seger[4], Alexis T. Bell[3], Karen Chan[6,c]

[1] *SUNCAT Center for Interfacial Science and Catalysis, Department of Chemical Engineering, Stanford University, Stanford, California 94305, United States*

[2] *SUNCAT Center for Interface Science and Catalysis, SLAC National Accelerator Laboratory, Menlo Park, California, 94025, United States*

[3] *Joint Center for Artificial Photosynthesis, Lawrence Berkeley National Laboratory, Berkeley, CA 94720, United States*

[4] *Surface Physics & Catalysis (SurfCat), Department of Physics, Technical University of Denmark*

[5] *Department of Chemical Engineering, University of California, Santa Barbara, Santa Barbara, California 93117, United States*

[6] *CatTheory Center, Department of Physics, Technical University of Denmark, Kongens Lyngby 2800, Denmark*

(Dated: 11 June 2019)

[a] Electronic mail: sringe@stanford.edu [b] Contributed equally to this work. [c] Electronic mail: kchan@fysik.dtu.dk

S1. CONTINUUM MODELING

The MPB equation for a 1:1 electrolyte (z:z and 1:z for Figure S17) is given in ref.[1] and was solved in this work using the finite element package COMSOL Multiphysics® .[2] An 80 μm cell length was used with a maximum element size of 8 μm. The double layer region was then more accurately resolved by a fine grid of maximum element size of 0.1 Å. We then solve the MPB equation on a fine two-dimensional parameter space of PZC and ion size a and interpolate this space using rectangular bivariate splines. This provides us with a continuous representation of the surface charge density as a function of the parameters $\sigma(\phi^{\mathrm{M,PZC}}, a)$.
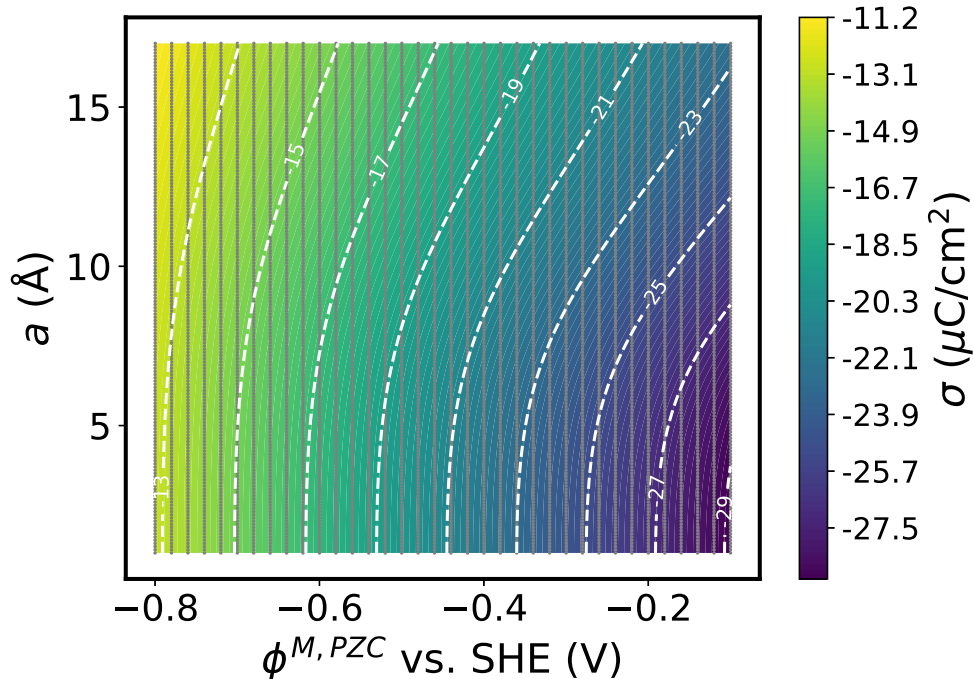

FIG. S1. Contour plot of the $\sigma(\phi^{\mathrm{M,PZC}}, a)$ function as obtained for a 1:1 electrolyte using the MPB model with $C_{\mathrm{gap}} = 25\,\mu\mathrm{F/cm}^2$ and ϕ^{M}=-1 V vs. RHE (pH = 7). Gray points denote points at which the MPB equation was explicitly solved, the contour is the spline interpolated function.

S2. DENSITY FUNCTIONAL THEORY CALCULATIONS

Density functional theory calculations of reaction energetics were carried out with a periodic plane-wave implementation and ultrasoft pseudopotentials using QUANTUM ESPRESSO version 6.1[3] interfaced with the Atomistic Simulation Environment (ASE).[4] We applied ultra-soft pseudopotentials and the BEEF-vdW functional, which provides a reasonable description of van der Waals forces while maintaining an accurate prediction of chemisorption energies.[5] Spin-polarized calculations were performed using plane-wave and density cutoffs of 500 and 5000 eV, respectively, as well as a Fermi-level smearing width of 0.1 eV. In general, adsorption energies were evaluated using symmetric (adsorbates on both sides of the slab) four-layered 3×3 supercells with all but a single outer layer on both sides constrained, 20 Å separation of the surface slabs, and [4×4×1] Monkhorst-Pack k-point grids.[6]

The SCCS implicit solvation model as implemented in the Environ QUANTUM ESPRESSO module[7] was used to model the presence of implicit water using the "fitg03" parameters for water (in a.u.: $\rho^{\mathrm{min}} = 0.0001$, $\rho^{\mathrm{max}} = 0.005$ as well a $(\alpha + \gamma) = 11.5\,\mathrm{dyn/cm}$). The surface charge density was modulated in order to simulate the response of adsorbate free energies to the presence of an electric double layer fields. A planar counter charge with a slab separation of 5 Å was applied to neutralize the simulation cell. A parabolic correction was applied in the Environ calculations to decouple the electrostatic interaction between the periodically repeated slabs.

The bulk dielectric permittivity in the solvation model was set to $\varepsilon_{\mathrm{b}} = 6\varepsilon_0$, where ε_0 is the vacuum permittivity. This value was rationalized by the following considerations. At elevated surface charge densities, the water layer close to Ag[8,9] and most metal electrodes[10–13] is ice-like, i.e. highly constrained exhibiting a low dielectric permittivity. The

dielectric permittivity dependence on an applied electric field has been suggested to follow the Booth model:[14]

$$\varepsilon_{\mathrm{b}}(|E|) = n^2 + (\varepsilon_{\mathrm{b}}(0) - n^2)\frac{3}{\gamma|E|}\left(\coth(\gamma|E| - \frac{1}{\gamma|E|}\right) \quad , \tag{S1}$$

with $n \approx 1.33$ the optical refractive index of water and $\gamma = 144\,\text{Å/V}$ the critical field parameter. Values were taken from ref.[15] The Booth model has been proven valid by molecular dynamics[16,17] and lattice Monte Carlo simulations.[18] Inserting this expression into the plate capacitor equation:

$$|E| = \frac{\sigma}{\varepsilon_{\mathrm{b}}(|E|)} \quad , \tag{S2}$$

we can then solve this non-linear equation for the electric field using a surface charge density of -20 μC/cm^2 that arises typically in our simulations at -1 V vs. RHE at Ag electrodes. The Booth model then gives us a value of around 6 for the relative dielectric permittivity. This low value agrees with recent experimental observations.[13,19,20] We therefore performed all following DFT calculations using this value.

All structures at all surface charge densities were relaxed using a BFGS line search algorithm until force components were less than 0.03 eV/Å. *CO$_2$ and *OCCO could only be stabilized with at least -1 e surface charge corresponding to around -20 μC/cm^2. We therefore extrapolated the free energy for smaller surface charge densities using the -1 e optimized geometry and single point calculations as described below representing an extrapolation along the diabate.

For the free energy diagram of CO production at Ag, zero-point energy and finite temperature corrections in the harmonic oscillator approximation were evaluated from the adsorbate vibrations at the Ag(111) surface at zero surface charge density using ASE. In the case of *CO$_2$, we used the optimized structure at -1 e of surface charge. We further applied an energy correction of 0.33 eV to the energy of CO$_{2,(g)}$ that was determined from fits to experimental gas phase reaction energetics.[5].

In the case of CO adsorption at Pt, we evaluated vibrations in the harmonic oscillator approximation from the *CO vibrations. The coverage was varied by using differently sized unit cells and keeping the k-point density constant ([4×4×1] Monkhorst-Pack k-point grids for the 3×3 unit cell[6])

S3. SURFACE CHARGE DENSITY DEPENDENCE OF ADSORBATES

Table S1 and the following figures show the surface charge dependence of formation energies of reaction intermediates without consideration of zero-point energy and finite temperature corrections. The pc-Ag surface charge dependence was taken from the (111) facet.

TABLE S1: Parabolic fits of $\Delta E(\sigma) = \Delta E(\sigma = 0) + a_\sigma\sigma + b_\sigma\sigma$, the surface charge density dependence of CO$_2$R reaction intermediate formation energies at different surfaces. *OCCO was referenced to 2× CO$_{(g)}$, *COOH to CO$_{2(g)}$ and H$_{2(g)}$, all remaining adsorbates to their gas phase equilvalent.

adsorbate	metal	facet	counter charge	d_H (Å)	$\Delta E(\sigma = 0)$ (eV)	a_σ (10^{-2} eV·cm^2/μC)	b_σ (10^{-4}eV·[cm^2/μC]^2)
*CO$_2$	Ag	111	PCC	5.0	0.76	2.86	-5.24
*CO$_2$	Ag	110	PCC	5.0	0.76	3.17	-6.55
*CO$_2$	Ag	100	PCC	5.0	0.64	2.77	-6.42
*CO$_2$	Ag	211	PCC	5.0	0.86	4.11	-4.28
*CO$_2$	Ag	111	PCC	4.0	0.76	2.21	-7.62
*CO$_2$	Ag	111	LPB	5.0	0.76	3.22	-3.30
*COOH	Ag	111	PCC	5.0	0.84	1.01	-4.33
*COOH	Ag	110	PCC	5.0	0.64	1.37	-2.03
*COOH	Ag	211	PCC	5.0	0.65	1.12	-5.37
*CO	Ag	111	PCC	5.0	-0.08	-0.60	-1.51
*CO	Ag	110	PCC	5.0	-0.20	-0.36	-1.63
*CO	Ag	211	PCC	5.0	-0.21	-0.33	-2.13
*CO	Cu	111	PCC	5.0	-0.49	-0.38	-1.1

*CO	Cu	100	PCC	5.0	-0.72	0.026	0.44
*CO	Cu	211	PCC	5.0	-0.74	-0.045	-0.55
*OCCO	Cu	111	PCC	5.0	0.083	2.64	-1.86
*OCCO	Cu	100	PCC	5.0	-0.37	3.93	0.25
*CO$_{br}$	Pt	111	PCC	5.0	-0.63	0.83	-0.84
*CO$_t$	Pt	111	PCC	5.0	-0.62	-0.58	-0.077

A. CO$_2$@Silver

Fig. S2 shows the surface charge density dependence of CO$_2$ at various Ag facets. We were able to stabilize CO$_2$ for all surface charges less or equal -1 e, which corresponds to a surface charge density of around -20 μC/cm^2 for the 3×3 unit cells that we used. In order to estimate the CO$_2$ adsorption energy at small surface charge densities, we applied two different extrapolation methods. As seen from the picture both methods agree in the the limit of large surface charge densities, but deviate substantially at smaller surface charge density. In the parabolic extrapolation case, we parabolically interpolated the relaxed CO$_2$ adsorption energy values at high surface charge density and used the fit function to extrapolate to smaller surface charge density regions. At zero charge, the parabolic method predicts CO$_2$ to be stable at the surfaces, in contrast to our observation of desorbing CO$_2$. The single point extrapolation method in contrast follows the diabate of the CO$_2$ adsorbate more strictly predicting a non-stable CO$_2$ geometry at zero surface charge density. We therefore apply it in the paper as we think it provides a more realistic estimate of the CO$_2$ binding energy at small surface charge density.
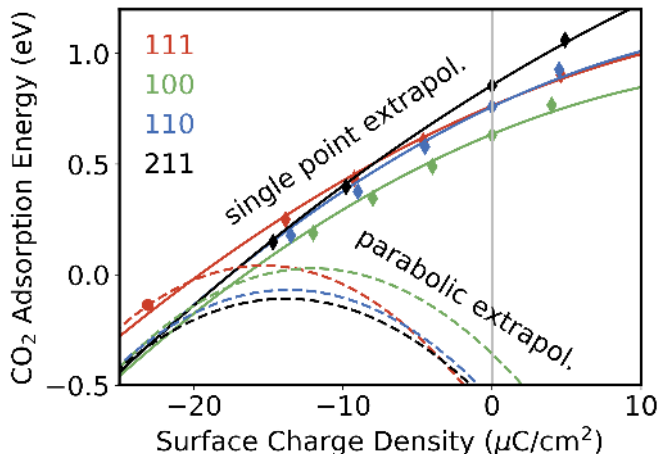

FIG. S2. Surface charge density dependence of CO$_2$ adsorption energy for the three Ag facets (111), (110) and (211). Shown are two ways to extrapolate the CO$_2$ binding energy to smaller surface charge densities, where CO$_2$ is not stable under standard conditions. The single point extrapolation method uses the optimized geometry at a total charge of -1 e (=-23 − -24 μC/cm^2) and performs single point calculations to approximate the energy at smaller surface charge densities. The parabolic extrapolation uses a parabolic fit of the relaxed high surface charge density geometries to extrapolate the energy. Filled circles indicate points where both the bare slab as well as the adsorbate+slab could be relaxed at the elevated surface charge density. Filled diamonds in contrast show points where single point calculations have been performed for the adsorbate+slab calculation using the -1 e relaxed charge calculation.

Fig. S4 shows the impact of different counter charge representations on the surface charge dependence. As obvious from the figure, the surface charge depedence is nearly fully independent of the chosen counter charge representation. The reason for this is that the main effect of the field stabilization comes from the vertical components of the electric field on the surface which are similar at a fixed surface charge density.
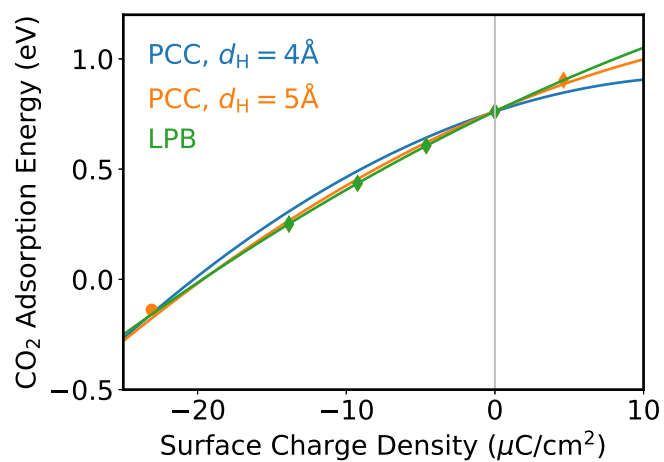
FIG. S3. Surface charge density dependence of the *CO$_2$ adsorption energy at the Ag(111) facet. Shown are different ionic counter charge representations, either as planar counter charge (PCC) at two different distances d_H from the surface or as approximated with the linearized Poisson-Boltzmann (LPB) model.
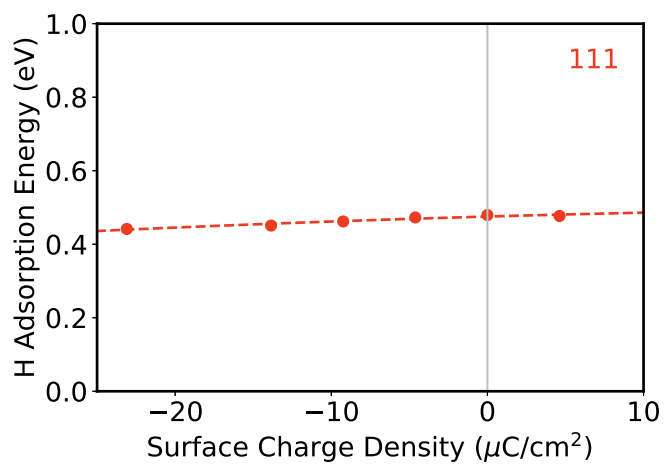
B. Other adsorbates @Silver

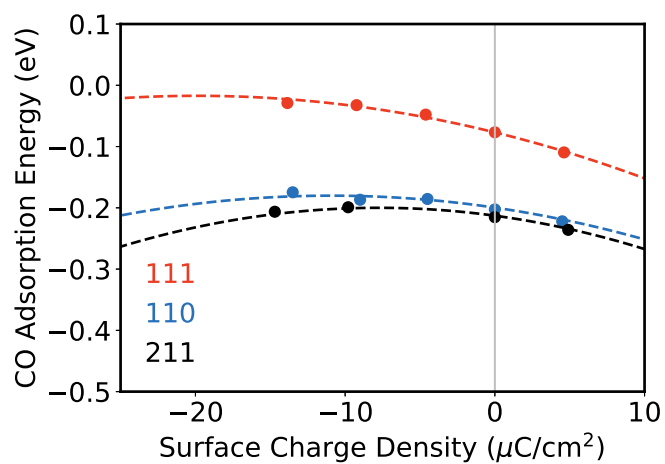FIG. S4. Surface charge density dependence of the *H adsorption energy at the Ag(111) facet.

FIG. S5. Surface charge density dependence of the *CO adsorption energy relative to $CO_{(g)}$ for the three Ag facets (111), (110) and (211).
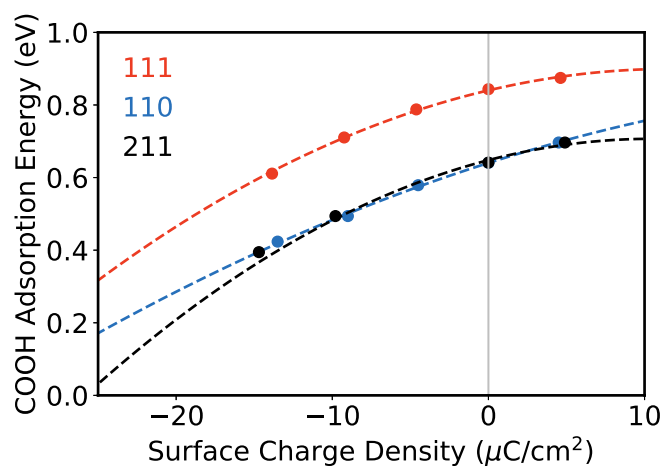
FIG. S6. Surface charge density dependence of the *COOH formation energy relative to $CO_{2(g)}$ for the three Ag facets (111), (110) and (211).
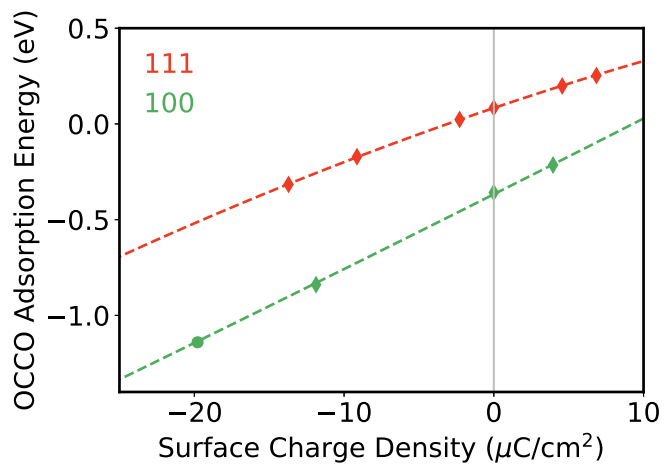
C. Copper

FIG. S7. Surface charge density dependence of the *OCCO formation energy relative to 2 $CO_{(g)}$ molecules at the (111) and (100) Cu facets. The (211) facet was found to be particularly difficult to numerically converge and is therefore not shown. The *OCCO adsorption energy was extrapolated via single point calculations for all total charges at surface charges >-1.0 e (=-20 − -24 $\mu C/cm^2$).
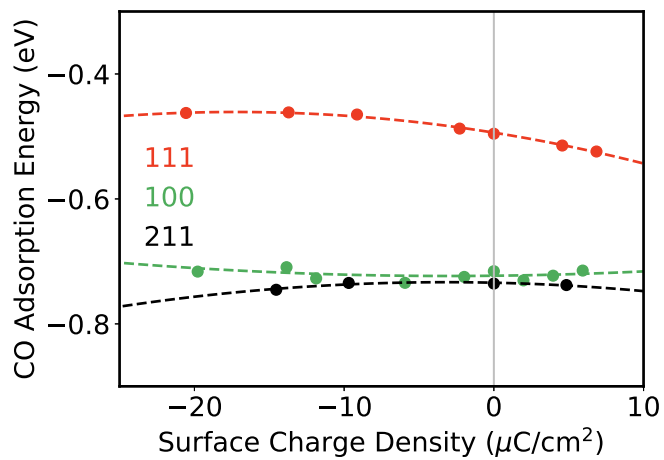

FIG. S8. Surface charge density dependence of the *CO formation energy relative to $CO_{(g)}$ at the (111), (100) and (211) Cu facets.
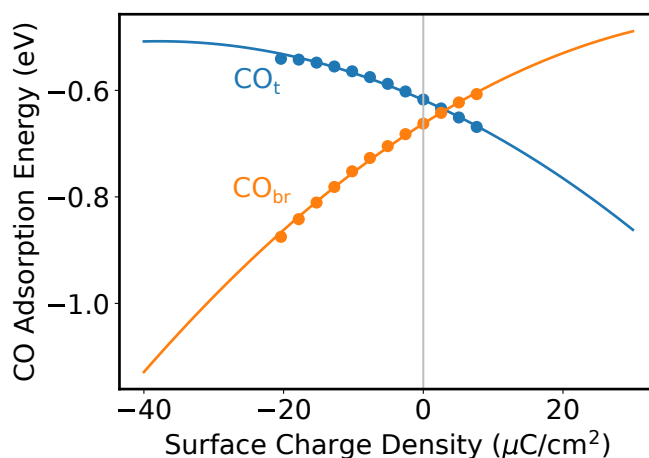
D. Platinum

FIG. S9. Surface charge density dependence of the *CO formation energy at bridge and top sites relative to $CO_{(g)}$ of the Pt(111) surface.

E. Free Energy Diagrams

Free energy diagrams were constructed using the surface charge density dependent formation energies of the previous section. Mapping from surface charge density to experimental applied potential was performed using the Robin boundary contitions and the MPB model with K^+ as a cation. The Computational Hydrogen Electrode (CHE)[21] was applied to further model the effect of the changing electrostatic potential of electrons in the metal electrode and the pH. Figure S10 shows the electric field-free and corrected free energy diagrams for CO_2 to CO reduction. We considered also the (211) surface as a typical stepped facet but applied the (111) PZC due to the relatively small density of steps on a typical poly-crystalline surface.
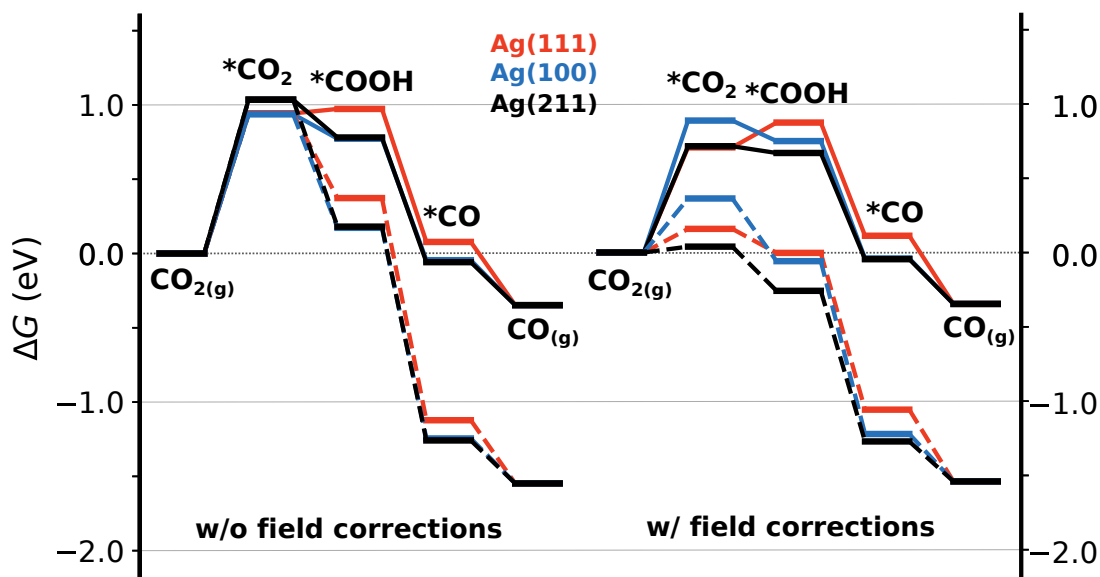

FIG. S10. Surface charge uncorrected ("w/o field correcitons") and corrected ("w/ field corrections") free energy diagram for CO_2 reduction at different Ag surfaces and -0.4 V (solid) and -1 V (dashed) vs. RHE.

S4. POTENTIAL OF ZERO CHARGE CALCULATIONS

A. PZC of pc-Ag

We found the experimentally measured PZC of poly-crystalline Ag to vary in a range of 0.1 V likely due to differences in the experimental fabrication process.[22] We therefore decided to evaluate a theoretical estimate for the PZC based on theoretical equilibrium crystal shapes according to the following equation:

$$\phi^{\mathrm{M,PZC}}(\mathrm{pc} - \mathrm{Ag}) = \frac{0.65 \cdot \phi^{\mathrm{M,PZC}}(\mathrm{Ag}(322)) + 0.2 \cdot \phi^{\mathrm{M,PZC}}(\mathrm{Ag}(100))}{0.65 + 0.2} \quad . \tag{S3}$$

The pre-factors in front of the (322) and (100) facets were taken from the equilibrium crystal shape of Ag from ref.[23]. Due to a lack of the experimental PZC of the (322) facet, the PZC's of both the (322) and the (100) facet were calculated using the Vienna ab initio Simulation Package (VASP).[24,25] In particular, we use the implicit solvation package VASPsol[26] which uses a solvent parametrization that predicts the PZC of metals when using the RPBE functional[27] in good agreement with experiment.[28] The original solvation parameters from ref.[26] were used with τ parameter in the solvation model set to zero. 1×1 symmetric unit cells with at least 5 metal layers and 100 Å slab separation were cut from the bulk optimized fcc lattice and used without further relaxation. PAW pseudo-potentials were further applied. The PZC was obtained from the Fermi level corrected by the Fermi shift (vacuum reference) and values of $\phi^{\mathrm{M,PZC}}(\mathrm{Ag}(100)$ = -0.66 V (experimental value: -0.621[22]) and $\phi^{\mathrm{M,PZC}}(\mathrm{Ag}(322))$ = -0.56 V were obtained.

B. PZC of *CO covered Pt(111)

The PZC of the *CO covered Pt(111) was determined using the Environ implicit solvation package[7] within QUANTUM ESPRESSO[3]. We used the fitg03 parameter set presented in ref.[7]. The *CO coverage was varied by varying the unit cell size, the k-point density was chosen as [12×12×1] for the 1×1 unit cell and kept constant for larger unit cells. 7 layers of metal atoms were used with a periodic slab separation of 30 Å. The BEEF-vdW xc-functional was further applied with energy and density cutoffs of 500 eV and 5000 eV, respectively, as well as ultrasoft pseudo-potentials. The slabs were fully relaxed in a similar way as described for the surface charge density dependent calculations above.
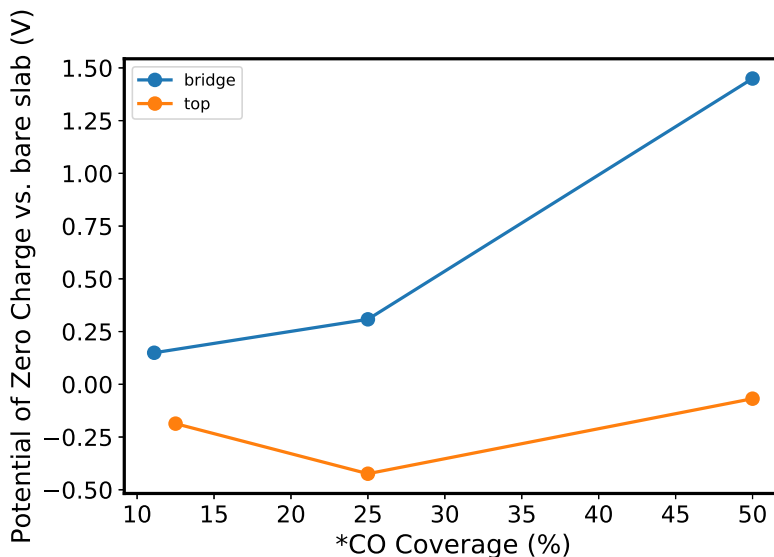

FIG. S11. PZC of *CO covered Pt(111) relative to the bare Pt(111) surface as a function of *CO coverage.

S5. CAPACITANCE MEASUREMENTS

The measured complex impedance was fitted by different circuit models. The RC circuit impedance is e.g. given by

$$Z = R + \frac{1}{i\omega C_{\mathrm{dl}}} \quad , \tag{S4}$$

where R is the solution resistance in series with the double layer capacitance and ω is the circular frequency. The RQ circuit introduces a constant phase element instead:

$$Z = R + \frac{1}{(i\omega)^\alpha Q} \quad , \tag{S5}$$

where using an $\alpha \neq 1$ can be understood as introducing frequency dispersion in the capacitance or making the capacitance less ideal leading to a non-vertical line in the Nyquist plot (cf. Figure S12 and S13).
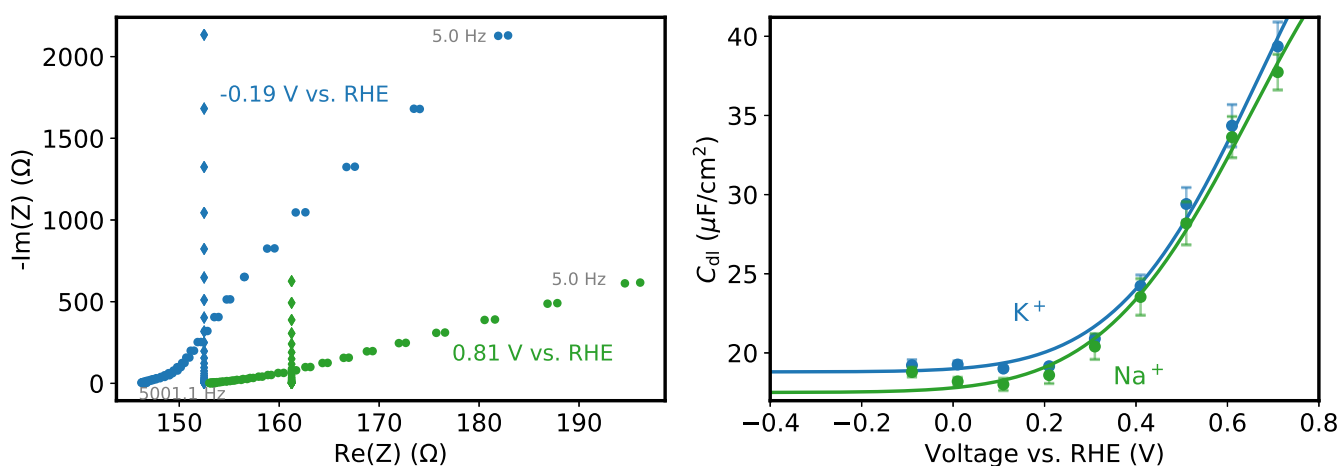

FIG. S12. *Left:* Imaginary vs. real part of the impedance plotted at various frequencies. Filled circles depict experimental data, diamonds the predictions of the RC circuit model. *Right:* Double layer capacitance as a function of applied potential.
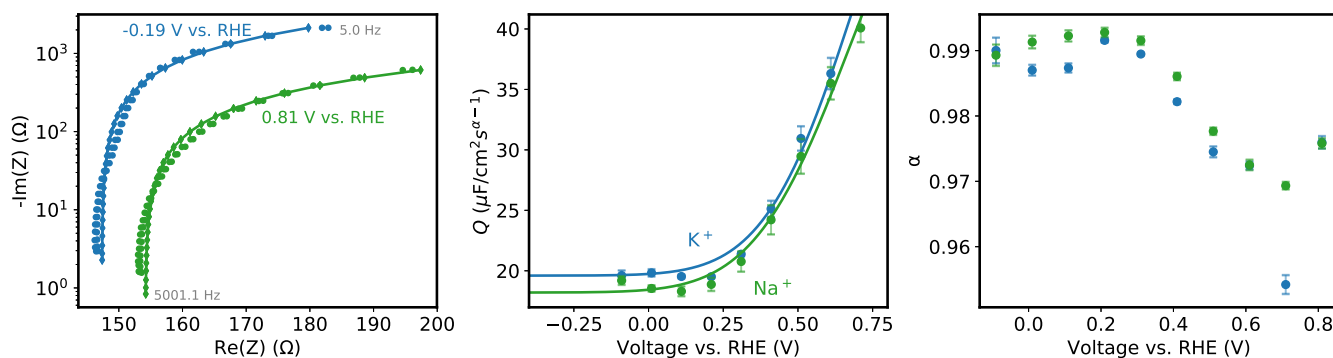

FIG. S13. *Left:* Imaginary vs. real part of the impedance plotted at various frequencies. Filled circles depict experimental data, diamonds the predictions of the RQ circuit model. *Center:* Q-constant phase element, *Right:* constant phase exponent α as a function of applied potential. Colors and symbols are as in Figure S12

We also tested more circuits including for example an adsorption resistance, but did not find any influence of this on the capacitance.

S6.   ION CORRELATION WITH HYDRATED ION RADII
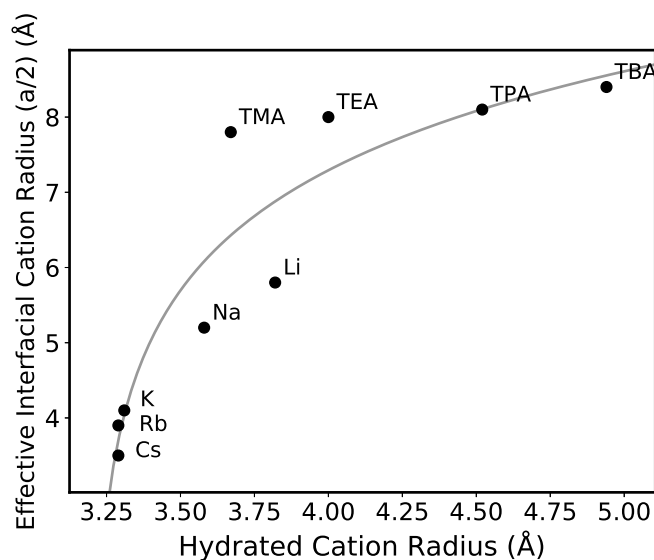

FIG. S14. Correlation of determined interfacial cation radii with bulk electrolyte hydrated cation radii.
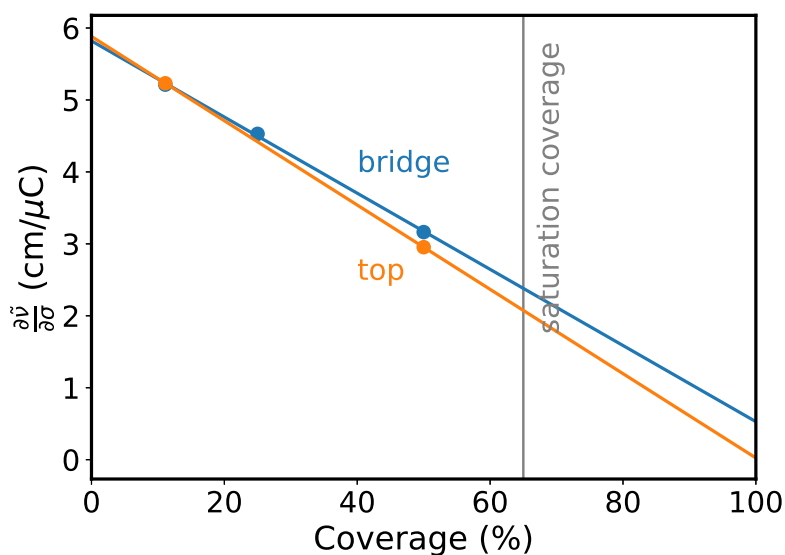
S7.   CO ADSORPTION @ PT

FIG. S15. Stark tuning rate of *CO at the bridge and top site at Pt(111) under electrochemical conditions.

S8.   CATION EFFECTS ON CO PRODUCTION @ AG(110)

Figure S16 shows the CO production rate at the different Ag surfaces. The data is here explicitly also shown with reference to Li^+ to show the deviation in the data for this cation. Li^+ is in particular difficult to treat experimentally, because atomically larger cations adsorb stronger and impurities therefore contribute nonequivalently more to the observed activity. Chelex resin can also not be used with Li-based electrolytes (due to Na contamination). This means the initial purity of the Li^+ electrolyte is lower and that it is susceptible to inadvertent contamination.
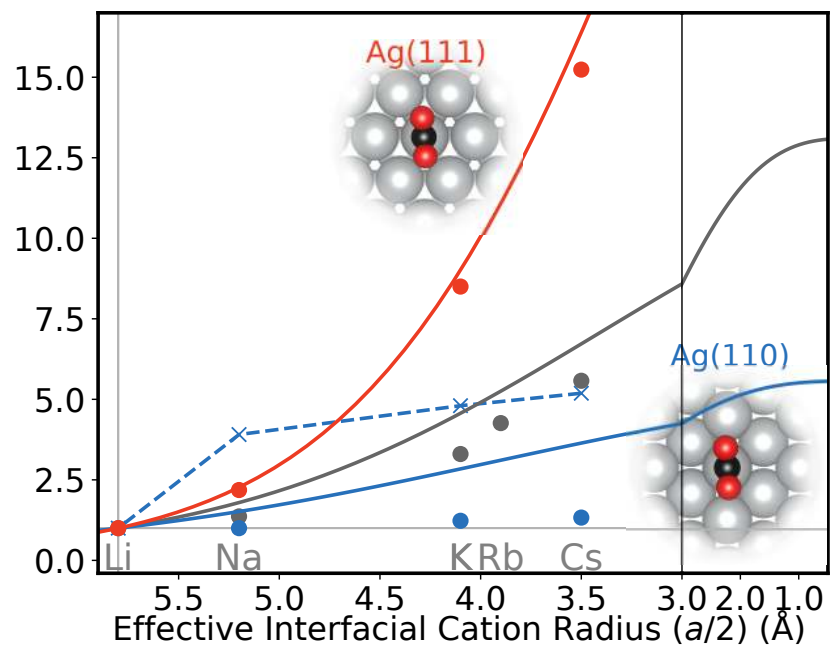
FIG. S16. CO partial current density at Ag(110), Ag(111) and poly-crystalline Ag at -1 V vs. RHE for different cations normalized to the CO current density in the Li$^+$ case. The Li$^+$ data point of CO current density at Ag(110) exhibited an anomalously low partial current density of CO correlating with a large partial current density increase of the HER. The dashed line illustrates that this leads to a constant shift of all data points of the other cations. We also plotted the Ag(110) data relative to Na$^+$ as in the main paper.
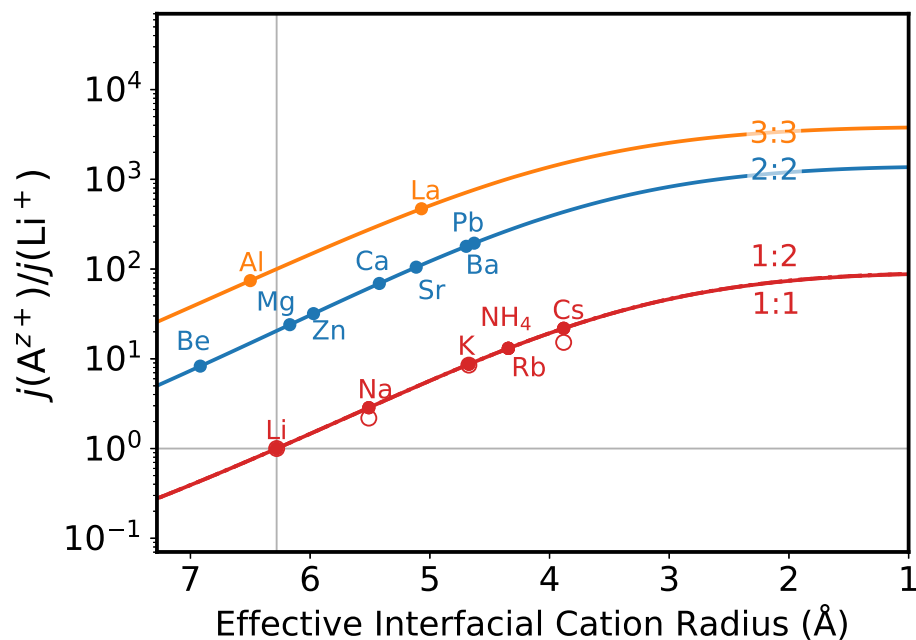
S9. CATION EFFECT PREDICTION

FIG. S17. Prediction of cation effects at the example of electrocatalytic CO_2 reduction on Ag(111) at -1 V vs. RHE using the determined interfacial ion size correlation for hydrated ions with the ionic crystal radius. The figure depicts the predicted CO partial current density for 0.1 M A_xB electrolytes having a cation:anion charge ratio of z:z_x as a function of the effective interfacial cation size relative to Li^+ as a cation. The empty circles represents data that was experimentally measured within this study.
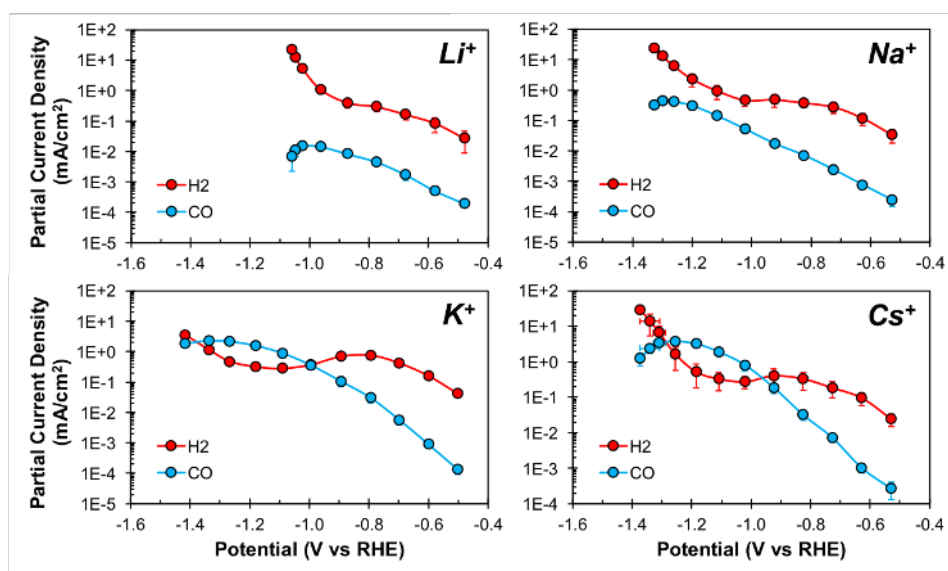
S10. EXPERIMENTAL DATA FOR CO$_2$R@AG FACETS

FIG. S18. Experimental polarization curves for CO_2R and HER at the (111) surface facet in 0.1 M bicarbonate solution.
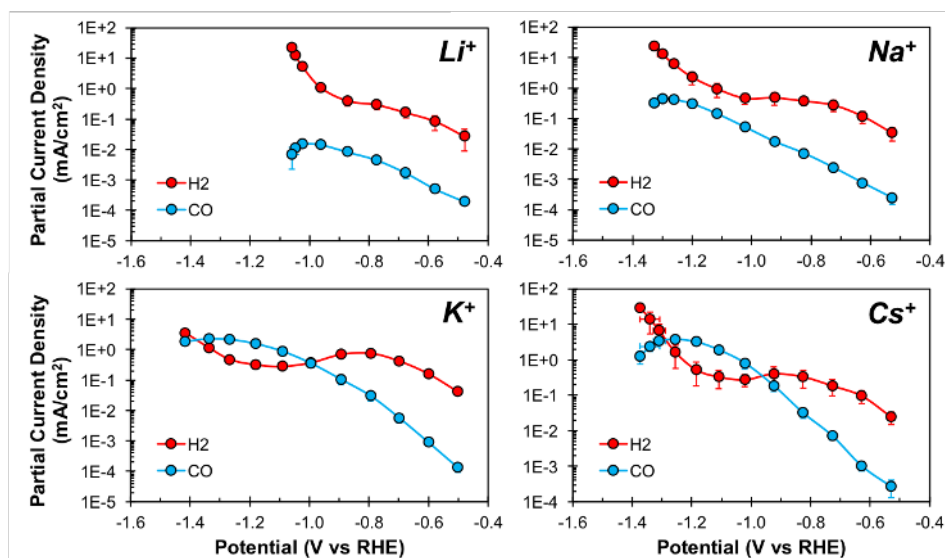
FIG. S19. Experimental polarization curves for CO_2R and HER at the (110) surface facet in 0.1 M bicarbonate solution..

[1] Borukhov, I.; Andelman, D.; Orland, H. Adsorption of large ions from an electrolyte solution: a modified Poisson–Boltzmann equation. *Electrochim. Acta* **2000**, *46*, 221–229.

[2] COMSOL Multiphysics v. 5.3a, COMSOL AB, Stockholm, Sweden. `http://www.comsol.com`.

[3] Giannozzi, P. et al. QUANTUM ESPRESSO: a modular and open-source software project for quantum simulations of materials. *J. Phys. Condens. Matter* **2009**, *21*, 395502.

[4] Hjorth Larsen, A. et al. The atomic simulation environment—a Python library for working with atoms. *J. Phys. Condens. Matter* **2017**, *29*, 273002.

[5] Studt, F.; Abild-Pedersen, F.; Varley, J. B.; Nørskov, J. K. CO and CO2 Hydrogenation to Methanol Calculated Using the BEEF-vdW Functional. *Catal. Letters* **2013**, *143*, 71–73.

[6] Monkhorst, H. J.; Pack, J. D. Special points for Brillouin-zone integrations. *Phys. Rev. B Condens. Matter* **1976**, *13*, 5188–5192.

[7] Andreussi, O.; Dabo, I.; Marzari, N. Revised self-consistent continuum solvation in electronic-structure calculations. *J. Chem. Phys.* **2012**, *136*, 064102.

[8] Toney, M. F.; Howard, J. N.; Richer, J.; Borges, G. L.; Gordon, J. G.; Melroy, O. R.; Wiesler, D. G.; Yee, D.; Sorensen, L. B. Voltage-dependent ordering of water molecules at an electrode–electrolyte interface. *Nature* **1994**, *368*, 444.

[9] Toney, M. F.; Howard, J. N.; Richer, J.; Borges, G. L.; Gordon, J. G.; Melroy, O. R.; Wiesler, D. G.; Yee, D.; Sorensen, L. B. Distribution of water molecules at Ag(111)/electrolyte interface as studied with surface X-ray scattering. *Surf. Sci.* **1995**, *335*, 326–332.

[10] Parsons, R. The metal-liquid electrolyte interface. *Solid State Ionics* **1997**, *94*, 91–98.

[11] Noguchi, H.; Okada, T.; Uosaki, K. Molecular structure at electrode/electrolyte solution interfaces related to electrocatalysis. *Faraday Discuss.* **2008**, *140*, 125–137.

[12] Beltramo, G.; Giesen, M.; Ibach, H. Anomalous Helmholtz-capacitance on stepped surfaces of silver and gold. *Electrochim. Acta* **2009**, *54*, 4305–4311.

[13] Fumagalli, L.; Esfandiar, A.; Fabregas, R.; Hu, S.; Ares, P.; Janardanan, A.; Yang, Q.; Radha, B.; Taniguchi, T.; Watanabe, K.; Gomila, G.; Novoselov, K. S.; Geim, A. K. Anomalously low dielectric constant of confined water. *Science* **2018**, *360*, 1339–1342.

[14] Booth, F. The Dielectric Constant of Water and the Saturation Effect. *J. Chem. Phys.* **1951**, *19*, 391–394.

[15] Wang, H.; Pilon, L. Accurate Simulations of Electric Double Layer Capacitance of Ultramicroelectrodes. *J. Phys. Chem. C* **2011**, *115*, 16711–16719.

[16] Yeh, I.-C.; Berkowitz, M. L. Dielectric constant of water at high electric fields: Molecular dynamics study. *J. Chem. Phys.* **1999**, *110*, 7935–7942.

[17] Fulton, R. L. The nonlinear dielectric behavior of water: comparisons of various approaches to the nonlinear dielectric increment. *J. Chem. Phys.* **2009**, *130*, 204503.

[18] Duan, X.; Nakamura, I. A new lattice Monte Carlo simulation for dielectric saturation in ion-containing liquids. *Soft Matter* **2015**, *11*, 3566–3571.

[19] Kornyshev, A. A.; Spohr, E.; Vorotyntse, M. A. In *Encyclopedia of Electrochemistry*; Bard, A. J., Ed.; Techn. Report no 14 to the office of Naval Research of Febr. 18, 1954; Wiley-VCH Verlag GmbH & Co. KGaA: Weinheim, Germany, 2007; Vol. 41; p 2307.

[20] Hou, Y.; Aoki, K. J.; Chen, J.; Nishiumi, T. Solvent Variables Controlling Electric Double Layer Capacitance at the Metal–Solution Interface. *J. Phys. Chem. C* **2014**, *118*, 10153–10158.

[21] Nørskov, J. K.; Rossmeisl, J.; Logadottir, A.; Lindqvist, L.; Kitchin, J. R.; Bligaard, T.; Jónsson, H. Origin of the Overpotential for Oxygen Reduction at a Fuel-Cell Cathode. *J. Phys. Chem. B* **2004**, *108*, 17886–17892.

[22] Trasatti, S.; Lust, E. In *Modern Aspects of Electrochemistry*; White, R. E., J. O'M. Bockris, B. E. C., Eds.; KluwerAcademic/PlenumPublishers: New York, Vol. 33.

[23] mavrl: crystalium. `http://crystalium.materialsvirtuallab.org/`, Accessed: 2019-4-9.

[24] Kresse, G.; Furthmüller, J. Efficient iterative schemes for ab initio total-energy calculations using a plane-wave basis set. *Phys. Rev. B Condens. Matter* **1996**, *54*, 11169–11186.

[25] Kresse, G.; Furthmüller, J. Efficiency of ab-initio total energy calculations for metals and semiconductors using a plane-wave basis set. *Comput. Mater. Sci.* **1996**, *6*, 15–50.

[26] Mathew, K.; Hennig, R. G. Implicit self-consistent description of electrolyte in plane-wave density-functional theory. **2016**,

[27] Hammer, B.; Hansen, L. B.; Nørskov, J. K. Improved adsorption energetics within density-functional theory using revised Perdew-Burke-Ernzerhof functionals. *Phys. Rev. B Condens. Matter* **1999**, *59*, 7413–7421.

[28] Goodpaster, J. D.; Bell, A. T.; Head-Gordon, M. Identification of Possible Pathways for C-C Bond Formation during Electrochemical Reduction of CO2: New Theoretical Insights from an Improved Electrochemical Model. *J. Phys. Chem. Lett.* **2016**, *7*, 1471–1477.